Numerical Simulation of Reynolds Number Effects in a Turbine Flow Meter

E. von Lavante, U. Banaszak**, T. Kettner*, V. Lötz-Dauer***

*Elster Production GmbH, Mainz-Kastell, Germany

**Institute of Turbomachinery, University of Essen, D-45127 Essen, Germany

Abstract - In the process of design optimization, computational fluid dynamics was used in the present work to better understand the effects of the Reynolds number on the accuracy of a typical turbine flow meter. The complex three-dimensional unsteady flow field in a one-stage turbine gas flow meter was studied by carrying out numerical simulations using the Navier-Stokes equations solver Fluent. The simulation of all the viscous effects as well as secondary flows, such as the flow in the tip gap and secondary and tertiary vortices in the blade to blade region required very high grid resolution but was necessary in order to capture the intricate features present in the flow field due to the Reynolds number variation. The results of three-dimensional numerical simulations with realistic geometry, including even small geometric features found in the production-type meter were obtained.

I. INTRODUCTION

Due to the circumstances given by today's growing energy consumption throughout the world and the opening of gas markets, the transportation and measurement of natural gas becomes more and more important. From an economical point of view of the customer and the vendor, the volume of sales of gas has to be measured as accurately as possible. With respect to that, the requirements imposed on the measuring systems are very high. One flow meter that fulfills all the given requirements and is capable of measuring very accurately even under high pressures in field use is the turbine flow meter.

In the past, most of the investigations of turbine flow meters were done analytically and experimentally. Several authors focused on the development of an equation of motion of the meter by relating the driving torques of the fluid to the friction torques due to friction of the fluid on the hub, in the tip gap or in the bearing [1, 6, 8]. Many investigations [3, 8, 9] studied the effect of pulsations or profile deformations on the accuracy of the meter. In the last two decades the self-correcting and self-proving gas turbine meters have been subject of intensive research. One working principle is based on the coupling of two rotors. A sensor rotor small distance downstream from the main rotor senses and responds to changes in the exit angle of the fluid leaving the main rotor [2, 5, 6, 7].

In more recent work the flow in a two-stage meter was investigated numerically by the present authors [4] using a two-dimensional cascade model consisting of both stages in order to reduce the computational time of the unsteady simulations. A DFT analysis of the unsteady behavior of the blade forces [4] confirmed the experimentally determined trends. Strong stator/rotor interactions, yielding a high variation of the unsteady blade forces in the second rotor were found, leading to modifications in the basic turbine flow meter design.

The goal of the present investigation was to investigate the sources of inaccuracies in the flow measurement at low volumetric flow rates. To this end, the influence of the Reynolds number was particularly considered. The work was carried out in several steps. First, an iterative procedure to minimize the moment about the rotational axis was implemented on a relatively fine grid to find the moment free speed of rotation. This optimization of the rotational speed was undertaken for all the flow cases, being the maximum volumetric flow (Q_{max}), the flow rates $Q = 0.1 \cdot Q_{max}$ and $Q = 0.25 \cdot Q_{max}$ at the operating pressure of 1 bar and $Q = 0.1 \cdot Q_{max}$ at 10 bar. The simulations were executed using air as the metered gas. In order to study the effect of the changing Reynolds number, the case of $Q = 0.25 \cdot Q_{max}$ was computed for air at 10 bar inflow static gauge pressure. The corresponding computational grid used in the present work had approximately $1.2 \cdot 10^6$ cells. Subsequently, once the proper operating condition was determined, the flow field within the flow meter was investigated numerically. The resulting deviation from a linear behavior was finally studied.

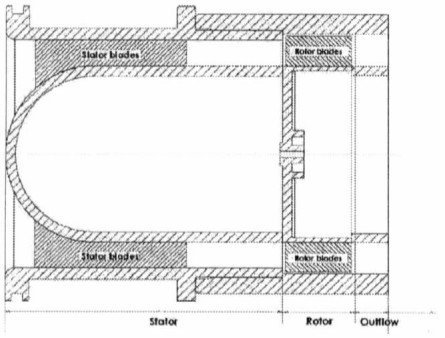

Figure 1: Cutaway drawing of the Elster TRZ DN80 turbine flow meter

II. PRESENT APPROACH

1.1 Choice of numerical tools.

Figure 1 shows a cutaway drawing of the turbine flow meter TRZ DN 80, manufactured by the Elster GmbH, that has been investigated in the present work. In order to make the flow simulation feasible, a few simplifying assumptions had to be made. In the original meter, there were 17 blades in the stator (flow conditioner) and 10 in the rotor. This design minimizes the danger of resonance, but requires the simulation of the entire meter, since the flow is periodic with respect to 2π. The present authors therefore assumed 20 blades in the stator and 10 blades in the rotor, employing the so called Reduced Blade Count approach. The flow field could now be treated as periodic in a segment consisting of 2 stator blades and one rotor blade. A view of the entire configuration is offered in Fig. 2, with the corresponding computational domain in the form of the grid displayed in Fig. 3. The hub of the meter is coloured by the contours of constant static pressure. The geometry of the paticular meter simulated here was kept as original as possible, including all irregularities such as steps, dents, gaps and grooves, since these could affect the flow and, therefore, the accuracy as well. The computational grid generation was accomplished using the GRIDGEN program, since it allowed the combination of structured and unstructured grids to be combined while being relatively easy to use (for more details, see the next section).

The flow solver selected for the present work was the Fluent system in version 6.x. Out of the many options available in this code, following combination was chosen:

- Accuracy in space was maintained at 2nd order for all the governing equations.
- Discretization in space was using the segregated scheme, since the flow was entering the meter at a maximum Mach number of Ma=0.04. It was, therefore, reasonable to assume that no nonlinearities existed in the flow field.
- The discretization in time was also 2nd order using an implicit subiteration in pseudotime. 20 iterations were judged sufficient.
- The working medium (air) was assumed to be an ideal compressible gas.
- The k-ϵ realizable turbulence model was used, employing wall functions where applicable. On the finer grids, no wall functions where necessary, since the resolution at the wall was better than $y^+ = 1$.

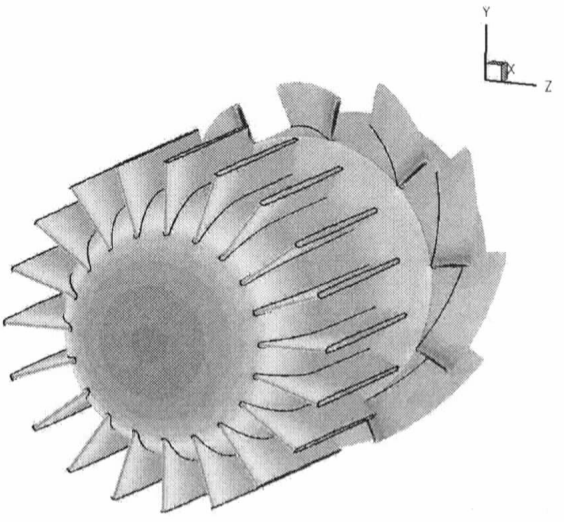

Figure 2: A view of the entire geometry assumed in the simulation.

The flow was assumed to be compressible since locally (at sharp edges, for example) the flow could expand to Mach numbers higher than Ma = 0.3. Only the truly unsteady mode of computation was considered, with an time accurate stator-rotor interface implemented. Nonreflecting boundary conditions had to be used throughout the computational domain. The computations were carried out on a cluster of PC-type workstations using the Linux OS. The cluster is connected by a high performance network, making a moderately parallelized computations possible.

1.2 Inflow conditions.

The flow meter selected for the present investigation had an annular inlet of D = 0.0775 m diameter. It was rated for maximum volumetric flow of $\dot{V} = 250m^3/h$. In the present simulations, four cases were considered: they are summarized in Table 1. The base case was for the maximum

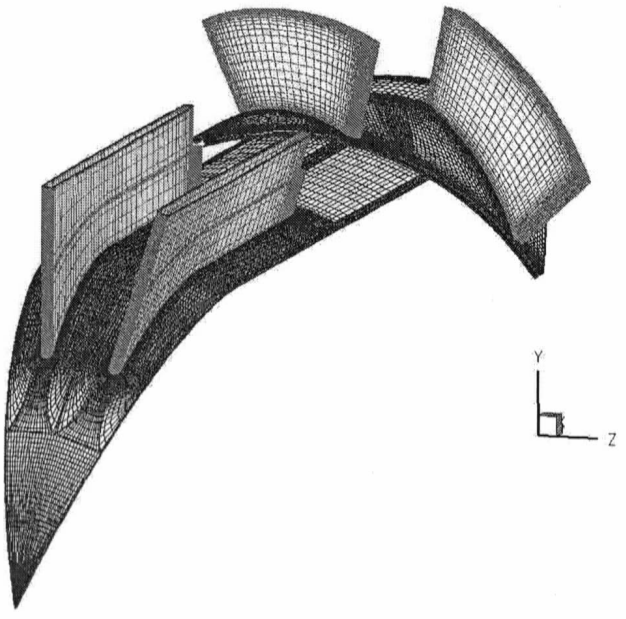

Figure 3: Surface grid used in the present simulations

volumetric flow Q_{max} with the mean inflow velocity was $u_{in} = 14.72m/s$, the static pressure $p = 1.01325 \cdot 10^5 Pa$ and the static temperature T = 293.15 K. The corresponding Mach number in the inflow was Ma = 0.04288 and the Reynolds number based on the diameter of the meter was $Re = 73.6 \cdot 10^3$. In the case of the smaller volume flow rates, the mean inflow velocity was reduced correspondingly, while the static conditions remained the same for the first three cases and were changed to 10 bar for the last case. The other flow variables were changed accordingly.

The incoming velocity profile was assumed to be symmetric fully developed turbulent flow according to Nikuradse. The profile was obtained by carrying out numerical simulation of a corresponding pipe flow in two dimensions. The incoming turbulence level was set to 5 percent. Pressure inlet and outlet conditions were used to yield the desired mass flow rates. This procedure required adjusting the outlet pressure to a proper preset value in several iteration steps, and was therefore very time consuming.

1.3 Computational grid.

As pointed out in previously, the emphasis of the present work was put on detailed analysis of the corresponding flow fields. Therefore, a two-dimensional configuration was judged insufficient due to its lack of any secondary and three-dimensional effects. On the other hand, severe restrictions were imposed due to the limited computational resources. The local RAM requirement had to be kept below 4.0 GB and the computational times should amount to approximately a week. On the other hand, the establishment of the correct mass flow and the optimization of the operating conditions (see next chapter) required several computations for each volume flow case. In view of these problems, a fairly fine grid with $1.2 \cdot 10^6$ cells that was carefully finetuned to the present application was generated.

A view of the entire grid can be seen in Fig. 3. There, the hub is shown in red and the rotor and stator blades are in green. The grid, shown in Fig. 2b had approximately $1,2 \cdot 10^6$ cells, covering all relevant boundary layers at the hub, the casing and the blades. The grid, consisting of 51 blocks, was mostly structured, with the only unstructured part at the centerline in front of the huband in the wake of the stator. The flow enters the meter axially in the positive x-direction (see Fig. 2a and 2b). It passes at first the central body (hub) with the guide vanes of the first stator, entering then the rotor. The speed of rotation of the rotor is input, given by the experimental data available for the corresponding case. As explained above, only two passages of the stator and of the rotor were simulated, so that the boundaries between each segment could be treated as periodic. During the postprocessing, the results from one passage were used to reconstruct the flow field in the remaining passages by copying.

In the circumferential direction, 58 grid points resolved the blade to blade plane on the medium grid. An exponential distribution close to the wall provided very small distances of the first cells to the wall so that at least 16 points in direction normal to the wall were within the boundary layer. The distance of the center of the first cell from the nearest wall corresponded to y^+ between 0.5 and 1.0. This implied that in the Fluent computations, the k-ϵ turbulence model was mostly used without wall functions. In the radial direction, 52 grid points were distributed over the height of the blade with exponential distributions close to the walls. 20 grid points were positioned in the radial direction in the tip gap between the rotor blades and the outer casing.

III. DETERMINATION OF SPEED OF ROTATION

During the initial phase of the present work it was found out that the flow in the rotor clearly indicated that there was a tangential force present, meaning that either the input rotational velocity or the throughflow were not correctly matched. This is possible, since the simulated flow meter is slightly different from the real one. The tangential force (lift on the baldes) resulted in a residual moment about the axis of rotation (x-axis). Clearly, the resulting flow field was not the actual one, as in reality the moment is very close to zero. The authors therefore decided to find a rotational speed that would match the given axial velocity (given

zero moment in the axial direction.

The rotational speed ω could be determined only iteratively. Before embarking on this endvor, one should realize that the procedure is very time consuming, since the resulting moment is first obtained by integration over the rotor blade surface and then has to be averaged over a time period that is much longer than the blade passing periodic time, $\Delta T \gg T$, where $T = \frac{1}{f}$ and f is the blade passing frequency.

As the simulation of three-dimensional, unsteady flows is very time consuming and requires large amounts of computer memory, the above iterative proccedure was carried out on the coarse grids only, with a subsequent simulation on the medium or fine grid. The influence of the local viscous effects was in this global consideration of secondary importance.

Assuming that the relationship between the mean coefficient of moment $\bar{c_m}$, obtained by averaging c_m in time, defined as:

$$c_m = \frac{M_{pr} + M_{visc}}{\frac{1}{2}\,\rho_{ref}\,c_{ref}^2\,A_{ref}} \qquad (1)$$

was linear within a small region close to $\bar{c_m} = 0$, the rotational speed ω_{max} was perturbed by $\pm 2\%$. In the above equation, M denotes moments due to viscous ($visc$) and pressure (pr) forces. The subscript ref denotes a reference state defined as the inflow conditions. A_{ref} is the area of the rotor blade calculated by the product of chord length and height of the blade.

The simualtion was run at least 10 blade passing periods, representing Δt, and then c_m was averaged over this time. The timewise history of the total moment coefficient c_m over one blade is given in Figure 4 for the maximum volume flow rate Q_{max} for three different rotational speeds ω: reference value given by the experiments and the two rotational speeds deviated by $\pm 2\%$. It is obvious that the timewise average value changes depending on the rotational speed. The simulated relationship of the resulting averaged coefficient of moment is shown in Figure 5. As assumed, the relationship is nearly perfectly linear, making an interpolation to $\bar{c_m} = 0$ rather easy. Similarly, the correct operating speed of rotation was determined for all the other volume flow rates of $Q = 0.1 \cdot Q_{max}$, $Q = 0.25 \cdot Q_{max}$ and $Q = 0.1 \cdot Q_{max}$ at 10 bar.

IV. RESULTS

4.1 Resulting flow field at $Q = Q_{max}$.

The corrected operating conditions were used to simulate the four volume flow rates. The inflow conditions are summarized in Table 1. As pointed out above, the simulations were performed on the medium grid with 1.2 million grid cells, as this grid was considered to be a reasonable compromise. The following discussion will concentrate

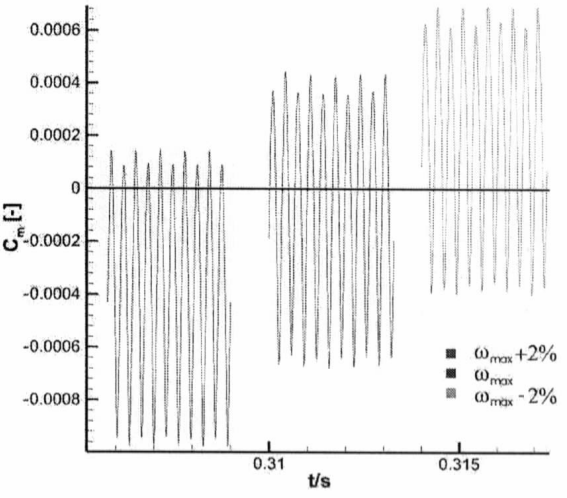

Figure 4: History of coefficient of moment c_m.

first on the flow details in various regions of the flow field for the case of Q_{max}. Obviously, at the given inflow conditions, the flow will be predominantly turbulent, and was simulated using the $k-\epsilon$ model in the entire configuration.

The static gauge pressure relative to the inflow static pressure is shown on the surface of the entire flow meter in Figure 6. As the flow enters the guide vanes, the cross-sectional area is reduced by the central body, accelerating the flow as indicated by the decreasing pressure on the hub of the central body. A stagnation point develops at the front of the central body. The unsteady fluctuations of the static pressure on the walls indicate that there is some influence of the rotor on the flow in the guide vanes. The region of stagnation point changes in size periodically with the rotor passing the stator vanes. There was no evidence of flow separation on the hub between the guide vanes, as the pressure uniformly decreases along its surface in the streamwise direction. A closer look at the static pressure contours on the rotor reveals an increasing stagnation pressure at the leading edge, indicating radial increase of the relative velocity. The stagnation pressure decreases in the boundary layers at the hub and tip. In particular, there is an significant pressure release at the tip due to the tip gap flow.

The flow field for the baseline configuration has been described in much more detail in [12]. There, an interested reader will find also a discussion of the velocity field and the tip gap flow. Besides, the secondary flow features in both the rotor and stator are pointed out and described.

4.2 Operating line for turbulent flow.

The resulting signal given by the total moment about the x-axis is shown in Fig. 7. It is very

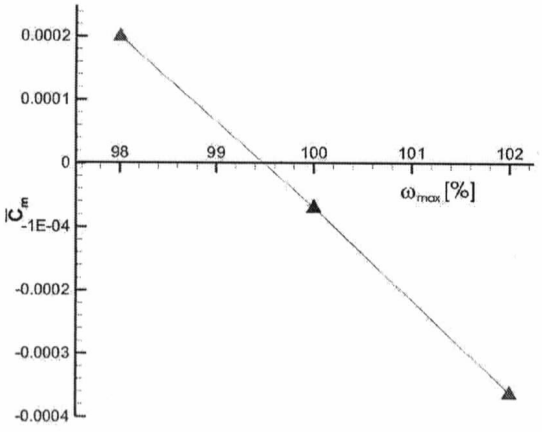

Figure 5: Mean value $\bar{c_m}$ as a function of ω for Q_{max}.

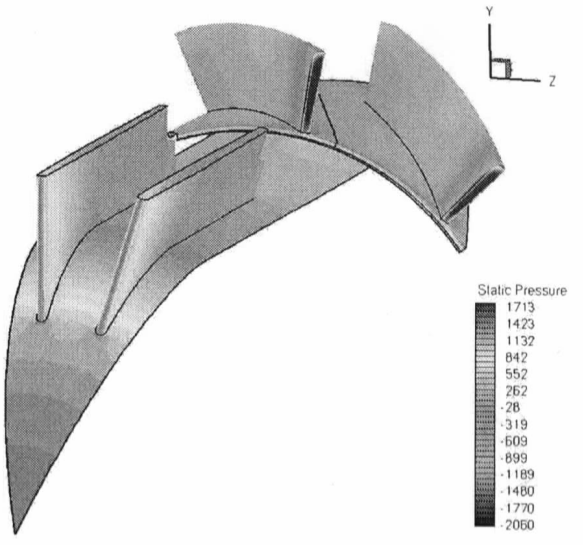

Figure 6: Static pressure distribution on the solid surfaces, $Q = Q_{max}$.

smooth, indicating no flow disturbancies upstream of the rotor. The DFT-analysis has shown that, as expected, the blade passing frequency was dominating. Similar results were obtained for the other three flow cases of $Q = 0.1 \cdot Q_{max}$, $Q = 0.25 \cdot Q_{max}$ and $Q = 0.1 \cdot Q_{max}$ at 10 bar. Plotting the dependence of the rotational speed ω as a function of the volumetric flow rate $\dot{V}$ results in the graph displayed in Fig. 8. At the first look, the curve seems to be perfectly linear. However, a closer study of the results reveals differences from the ideal line showing errors that are of the order of magnitude of 1%. The deviation of the simulated frequency from the linear behavior is plotted as an error in Fig. 9. Comparing the simulated results with the experimental data as well as operational experience shows that the error has the correct magnitude but the wrong tendency. It is fairly well known that at small flow rates the error first rises due to flow phenomena before it rapidly drops because of increasing influence of rotational moment due to mechanical friction. The reason of this fundamental disagreement has to be sought in the character of the flow within the boundary layer. It has been already stated that the free stream turbulence in the inflow was 5%. This leads to the assumption that flow in the stator will relatively soon transition from laminar to turbulent despite the favourable pressure gradient at this location. This conclusion is most certainly correct for the flow at $Q = Q_{max}$, since the Reynolds number was 7410^3. However, at the much smaller flow rates of $Q = 0.25 \cdot Q_{max}$ and, in particular, $Q = 0.1 \cdot Q_{max}$, the flow will be at least in a significant portion of the flow field laminar before it transitions to turbulent. It was, therefore, decided to repeat the simulations of $Q = 0.1 \cdot Q_{max}$ and $Q = 0.25 \cdot Q_{max}$ under the assumption of laminar flow.

4.3 Laminar flow simulations.

The laminar flow simulations had to be carried out assuming that the laminar flow was present in the entire computational domain, since the simulation program Fluent does not allow partially turbulent flow. The frequency obtained by the same procedure outlined in Chapter III and is included in Fig. 8. The deviations from the operating line are again so small that they can not be distinguished from this picture. However, including the laminar results in the error plot in Fig. 9 shows that this time, the error displays the correct tendency, being in the positive range of values as the voumetric flow becomes smaller. At $Q = 0.1 \cdot Q_{max}$, the flow is suspected to be predominantly laminar (at least upstream of the rotor), so that the realistic error for this flow rate would be approximately +1.5%, which is completely realistic. At $Q = 0.25 \cdot Q_{max}$, the simulated error amounts to be about 3.2%, a value that is too large for the given meter. Comparing the Reynolds numbers for the two cases, Re = 7.410^3 for $Q = 0.1 \cdot Q_{max}$ and Re = 18.510^3 for $Q = 0.25 \cdot Q_{max}$, leads to the conclusion that at $Q = 0.25 \cdot Q_{max}$ rate, the Reynolds number is sufficiently large to cause the flow to transition from laminar to turbulent well before entering the rotor, meaning that the flow field will be of "mixed" character, partially laminar and partially turbulent. The authors do not want to suggest that one should simply "average" the two error values for the turbulent and laminar computations, but the truth will be somewhere between the two extremes of −1.5% and +3.2%, again falling into the correct range of values.

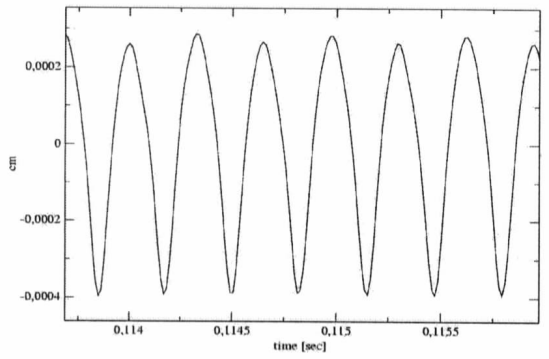

Figure 7: Total moment on the rotor blade, $Q = Q_{max}$.

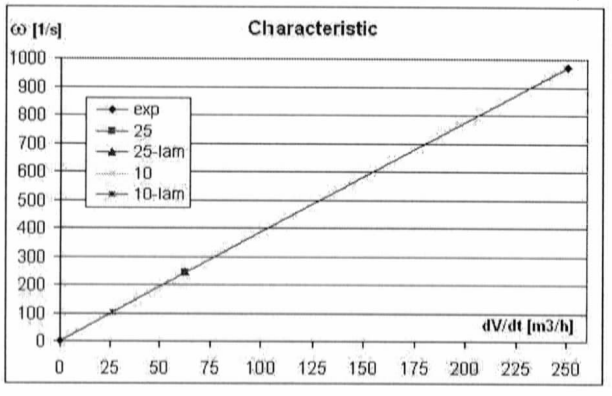

Figure 8: Operating line for the flow meter under consideration.

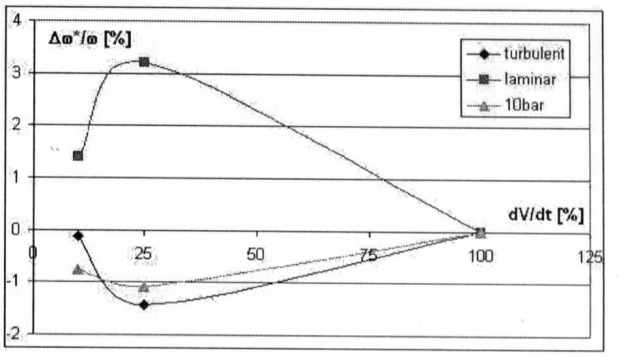

Figure 9: Metering error as a function of the flow rate.

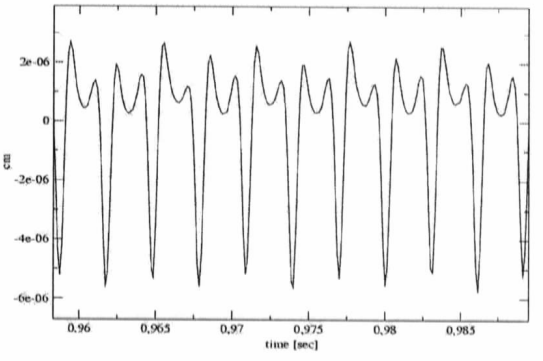

Figure 10: Total moment on the rotor blade, $Q = 0.1 \cdot Q_{max}$, laminar flow.

At the higher pressure of 10 bar, the flow will be certainly turbulent, since the Reynolds number is of the same magnitude as in the case $Q = Q_{max}$. Clearly, all the simulations at this higher pressure were carried out assuming fully turbulent flow. The resulting error is also included in Fig. 9. The error curve is in this case much flatter, being in reasonable agreement with the experimental observations.

4.4 Differences between laminar and turbulent flow simulations.

What is the reason for the differences between the flow fields in general and the resulting deviation from the linear operating behavior in particular? First indication of the differences is obtained by comparing the signals from the laminar (Figure 10) and turbulent (Figure 11) computations. The turbulent signal is again, as in the case of $Q = Q_{max}$, very smooth and regular, oscillating with exactly the blade passing frequency. The laminar signal, in contrast, is very irregular, with a more or less periodic disturbance at the "peack" of the total momentum. The minimum of the rotational moment ocurres in the wake of the stator blades, so that consequently the maximum value is reached when the rotor blade is in the middle of the stator passage. One would not expect a disturbance at this location.

The explanation can be found in Figure 12. Here, the velocity vectors of the absolute velocity in the blade-to-blade plain are plotted, superimposed on the contours of total velocity magnitude. Clearly visible is the wake behind the guide vanes, shown in dark blue. Equally visible are the boundary layers on all the solid surfaces. The flowfield in the plain perpendicular to the passage channel is dominated by secondary flow features. The two secondary vortices rotating in opposite directions are formed by the turning of the boundary layer along the hub. They give rise to a stagnation point on the upper surface - the casing of the meter - in the middle of ths passage channel. As is the case with every stagnation point, the pressure increases

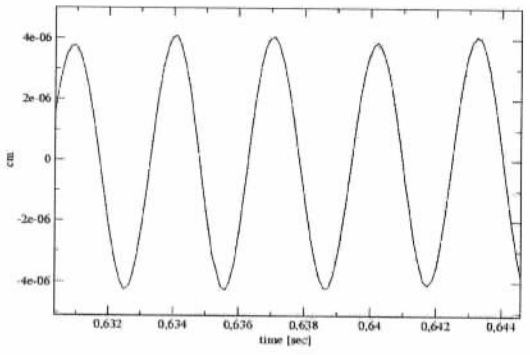

Figure 11: Total moment on the rotor blade, $Q = 0.1 \cdot Q_{max}$, turbulent flow.

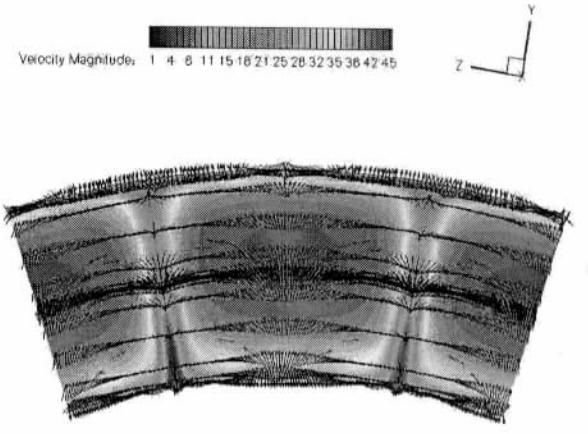

Figure 12: Vectors of the absolute velocity just downstream of the stator blades, $Q = 0.1 \cdot Q_{max}$, laminar flow.

at this location, creating a local adverse pressure gradient that is affecting the flow in the boundary layer.

Turbulent boundary layers are inherently more stable and are more difficult to separate. Laminar boundary layers are less stable and therefore more prone to separate than turbulent boundary layers. In the present case of $Q = 0.1 \cdot Q_{max}$, the flow is laminar at the location of the midchannel stagnation point and therefore sensitive to the pressure rise at this position. The adverse pressure gradient leads to a boundary layer separation upstream of the rotor. The separated flow formed a wake of low energy fluid that was convected downstream until impinging on the rotor. The low velocity fluid in the axial direction altered the velocity triangle such that the relative incidence angle moved in the positive direction, thus causing the drop in the total moment about the x-axis seen in Figure 10. In all the cases of turbulent boundary layers, the flow remained attached and the signal displayed no irregularities.

The flow field in the guide vane passage channel is shown in more intricate detail in [12]; this publication should be consulted for more information about the physics of the flow.

V. CONCLUSIONS

In the present study the flow field in the Elster TRZ DN80 turbine flow meter was investigated by three-dimensional numerical simulations for four different operating conditions. The simulations were carried out using the solver FLUENT version 6.x. The resulting three-dimensional unsteady flow fields displayed many detailed features that made the explanation of several empirically observed phenomena possible. The novel procedure to determine the moment-free operating conditions worked well and was essential for obtaining realistic results. The accuracy of the determination of the operating conditions allowed the computation of the measurement error as a function of the volumetric flow.

The errors were assumed to be deviations from the linear behavior of the meter. They were discussed in some length and were shown to be caused by the transition of the boundary layer flow from laminar to turbulent.

It has been demonstrated that at least one possible reason for the irregularity of output signals in the laminar case was the secondary flow in the stator. The secondary vortices formed a stagnation point on the upper casing which, in turn, caused in the laminar case a flow separation.

Future work will concentrate on the determination of the location of the transition in the stator passage, allowing a mixed simulations with laminar flow upstream of the transition and turbulent flow downstream of it.

Table 1: Summary of inflow parameters.

flow variable	Q_{max}	$0.25 \cdot Q_{max}$	$0.1 \cdot Q_{max}$	$0.1 \cdot Q_{max} 10bar$
flow rate	250 m^3/h	62.5 m^3/h	25 m^3/h	25 m^3/h
temperature	293.15	293.15	293.15	293.15
velocity	14.72 m/s	3.68 m/s	1.47 m/s	1.47 m/s
pressure	1 bar	1 bar	1 bar	10 bar
Re	$74 \cdot 10^3$	$18.5 \cdot 10^3$	$7.4 \cdot 10^3$	$74 \cdot 10^3$

References

[1] Baker, R. C., "Turbine Flowmeters: II. Theoretical and Experimental Published Information", Flow Measurement and Instrumentation, 4(3), pp. 123-144, 1993.

[2] Gestler, D. J., "The Auto-Adjust Turbo-Meter and how it Developed", Pipeline Gas Journal, July, 1980.

[3] van der Kam, P. M. and van Dellen, K., "The Effect of Double Bends out of Plane on Turbine Meters", Flow Measurement and Instrumentation, 2, pp. 61-68,1991.

[4] von Lavante, E., Hüwener, T., Ernst, R. and Schieber, W., "Numerical Investigation of the Flow Field in a 2-Stage Turbine Flow Meter", Flow Measurement 2001, Glasgow, May 2001.

[5] Lee, W. F. Z., Blakeslee, D. C., and White, R. V., "A Self-Correcting and Self-Checking Gas Turbine Meter", Journal of Fluids Engineering, 104, pp. 143-149, 1982.

[6] Lee, W. F. Z., and Karlby, H., "A Study of Viscosity Effects and Its Compensation on Turbine-Type Flowmeters", Journal of Basic Engineering, Transactions ASME, 82, pp.717-728, 1960.

[7] Lee, W. F. Z., et al., United States Patent, No. 4,305,281. Rockwell Int. Corp., 1981.

[8] Lehmann, N., "Dynamisches Verhalten von Turbinenradgaszählern", Das Gas- und Wasserfach, 131(4), pp. 160-167, 1990.

[9] Mickan, B. et al., "Die Fehlerverschiebung eines Turbinenradzählers in Abhängigkeit vom Anströmprofil", PTB-Mitteilungen, 106(2), pp. 113-124, 1996.

[10] Perpeet, S., "Numerische Simulation von Strömungsfeldern um Durchfluß-Meßanordnungen", Dissertation, Universität Essen, 2000.

[11] Yao, J., "Numerische Simulation der Multi-Dimensionalen Strmung in Kolbenmotoren", Dissertation, Universität Essen, 1997.

[12] von Lavante, E., Lazaroski, N., Maatje, U., Kettner, T., and Lötz-Dauer, V., "Numerical Simulation of Unsteady Three-Dimensional Flow Fields in a Turbine Flow Meter", Proceedings of the 11th Int. Conference on Flow Measurement FLOMEKO 03, Groeningen, Netherlands, 2003.